small structures
www.small-structures.com

Planar Nb_nO_m Clusters on the Au(111) Surface

Shuqiu Wang, Yuhan Zhu, Maxime Van den Bossche, Jacek Goniakowski, Claudine Noguera, and Martin R. Castell**

Planar oxide atomic clusters are of considerable scientific interest because of their potential for enhanced catalytic activity versus their three-dimensional counterparts. This enhancement is the result of the substrate stabilizing novel planar configurations that have an extensive periphery where catalytic reactions can occur. A class of planar Nb_nO_m atomic clusters that are synthesized by the evaporation of metallic Nb onto an Au(111) substrate in an ultrahigh vacuum environment and subsequent oxidation at elevated temperatures is reported. The atomic structures of the clusters are determined using a combination of scanning tunneling microscopy and density functional theory. The clusters are composed of structural units with four-, five-, and sixfold rotational symmetry and these units can assemble to form larger planar clusters. The theoretical comparison of supported structures with their hypothetical freestanding counterparts shows that the atomic and electronic structures of the oxide clusters are significantly altered by the interaction with the Au substrate. The substrate effects include interfacial charge transfer and structural relaxation to relieve the strain in the Nb-O bonds. The substrate interactions also reduce the energy differences between clusters of different configurations and this enables the coexistence of a large variety of cluster configurations.

1. Introduction

Supported oxide nanoclusters at submonolayer coverage are attractive systems for the investigation of catalytic mechanisms in chemical reactions,[1,2] and are effective model systems for developing a physical understanding of "magic size effects" in the search for optimized catalyst materials.[3–5] The interaction between the cluster and the substrate also frequently reveals interesting physical phenomena relevant to the understanding of inverse catalyst systems.[6–10] Oxide clusters are of the order of a few nanometers in size with crystal structures, stoichiometries, and physical properties that are frequently distinctly different from bulk crystal phases. Novel structural, chemical, and electronic properties have been observed for a variety of supported oxide clusters of V, Fe, Co, Ti, Nb, Mo, W, Mg, and Ni.[5,8,11–17]

The metal supports also have a significant influence on the oxide clusters. Strong cluster–substrate interactions significantly alter the inherent atomic structure of the clusters. For example, a V_6O_{12} cluster is predicted to form a tetrahedral cage structure in the gas phase but forms a planar structure on metal supports in experiments.[18,19] The unsupported V_6O_{12} cluster has a triangular prism structure that is composed of one V_3O_3 six-membered ring connected to one V_3O_6 six-membered ring through three bridging oxygen bonds.[19] A Rh(111) supported V_6O_{12} cluster consists of six V atoms located in Rh(111) threefold hollow sites, six O atoms located in Rh on-top positions, and six dangling O atoms bonded to each V atom.[11,18] The planar cluster structure is stabilized by the strong interaction between the V_6O_{12} cluster and the Rh(111) substrate. Similarly, the structure of a Nb_3O_7 cluster is significantly modified when it is supported on a Cu(111) surface.[17] An unsupported Nb_3O_7 cluster has a hexagonal pyramid structure consisting of three Nb atoms and three bridging O atoms in the basal plane, and an O atom at the apex.[20] The supported Nb_3O_7 cluster has a planar structure that contains three Nb atoms located close to Cu(111) bridge sites, four O atoms located in Cu on-top positions, and three dangling O atoms bonded to each Nb atom.[17] Major substrate effects on the cluster structures have been observed in Nb, Mo, Ti, and W oxide clusters on Cu(111) and Cu_2O/Cu(111),[17,21] Ni oxide clusters on MgO/Ag(100),[13] W_3O_9 on Cu(110)-O(2×1),[22] and TiO_x clusters on Au(111).[16] The substrate effects include changes of the cation oxidation states, structural distortions of the cluster and support, and modification of the interfacial electronic structure of both the cluster and the substrate.

Here, we report on an investigation of the atomic structure and thermodynamic stabilization mechanisms of planar Nb oxide clusters on Au(111). Because Nb has stable oxidation states +2, +3, +4, and +5, this gives rise to various Nb-O coordination

S. Wang, Y. Zhu, M. R. Castell
Department of Materials
University of Oxford
Parks Road, Oxford OX1 3PH, UK
E-mail: shuqiu.wang@physics.ox.ac.uk; martin.castell@materials.ox.ac.uk
M. Van den Bossche, J. Goniakowski, C. Noguera
Paris Institute of Nanosciences
CNRS-Sorbonne Université
UMR 7588, INSP, F-75005 Paris, France
The ORCID identification number(s) for the author(s) of this article can be found under https://doi.org/10.1002/sstr.202300141.

DOI: 10.1002/sstr.202300141

motifs, which can in turn result in the formation of oxide clusters with a large range of stoichiometries and structures. In this article, we report the discovery of a wide variety of planar Nb oxide clusters on Au(111) using scanning tunneling microscopy (STM). The clusters can be separated into distinct groups depending on their symmetry. Modeling the clusters using density functional theory (DFT) demonstrates the significant influence of the substrate on the atomic structure, stoichiometry, cohesion energy, and electronic structure of the oxide clusters.

2. Results and Discussion

2.1. STM Imaging of Nb_nO_m Atomic Clusters on Au(111)

Figure 1a shows an Au(111) surface following Nb deposition at room temperature and annealing in 10^{-7} Pa O_2 at 400 °C. The surface is covered by approximately 0.25 monolayer (ML, where 1 ML coverage is defined as corresponding to an Au surface fully covered by a honeycomb Nb_2O_3 monolayer) of NbO_x. The two main types of nanostructures are atomic clusters and monolayer regions with a honeycomb (2×2) Nb_2O_3 structure.[23–25] The atomic clusters consist of several bright protrusions and their widths range from sub-nanometer to a few nanometers in size. The (2×2) honeycomb structure is a well-ordered monolayer film in perfect registry with the Au(111) substrate.[23,24,26,27] The honeycomb structure serves as an excellent reference and calibration lattice to determine the exact periodicity and orientation of the other structures (Section S2, Supporting Information). The atomic clusters are imaged in STM to be only approx. 0.2 to 0.3 Å higher than the (2×2) honeycomb monolayer film, and thus the clusters are in all likelihood also planar monolayer structures. A significant variety of Nb_nO_m atomic clusters are randomly distributed on the Au(111) surface. These atomic clusters are stable on the Au surface at low Nb coverage and in the temperature range from room temperature to 600 °C. Annealing the oxide clusters to higher temperatures up to 700 °C in oxygen atmosphere results in the honeycomb (2×2) structure and triangular nanocrystals (Section S3 and Figure S2, Supporting Information). The Au(111) herringbone reconstruction is lifted underneath the oxide nanostructures and distorted in the bare regions (Figure 1a).

The clusters consist of structural units that can either appear on their own, as in Figure 1b–e, or the units can fuse together to form larger clusters such as those that are visible in parts of Figure 1a. The most common structural units consist of four, five, or six bright spots, shown at high magnification in Figure 1b–e. For the clusters where the orientation can be determined (Section S2, Supporting Information), it matches the orientation predicted by modeling (Figure 1f–i). Each of the bright spots is associated with a Nb atom (a detailed structural analysis is discussed in the next section). The clusters can thereby be categorized into bonding symmetry-related groups. The nomenclature of each cluster is made up of the number of structural units (if more than one), the size of the structure within the units, and the total number of Nb atoms. The way of distinguishing the "size of the structure within the units" that we have adopted is to use the letter Q for quad (fourfold), P for penta (fivefold), and H for hexa (sixfold). To demonstrate an example of the nomenclature Figure 1b shows a Q4 cluster, representing fourfold bonding symmetry (Q) consisting of four (4) Nb atoms. Alternatively, a structure termed as a 2Q7 cluster in Figure 1a consists of two units of fourfold rings (Q) that together have seven Nb atoms in the cluster. In our extensive study, where we classified over 1000 clusters, the single Q4 and P5 clusters are the most common, followed by the H6 cluster. We will now examine each of these cluster groups in turn.

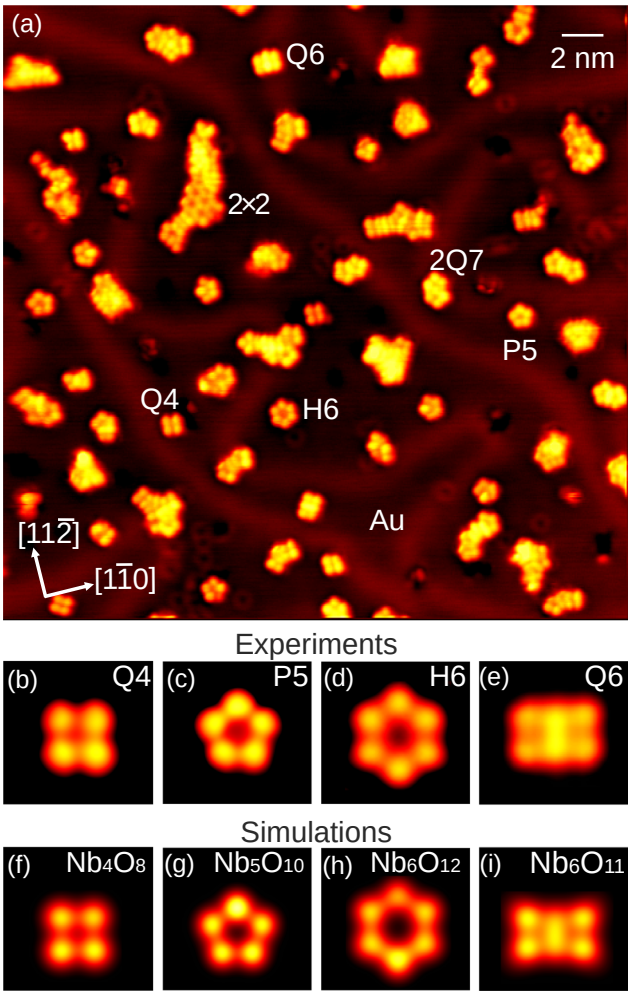

Figure 1. STM images of niobium oxide atomic clusters grown on Au(111). a) Nanostructures at a coverage of 0.25 ML following Nb deposition at room temperature and annealing in O_2 at an elevated temperature. Atomic clusters with four- (Q4 and Q6), five- (P5), and sixfold (H6) symmetry can be seen. The STM image is generated from 11 frames using multiple frame averaging (MFA) to enhance the signal-to-noise ratio, details described in the Supporting Information (Section S1). The image width is 30 nm. b–e) Close-up views of the frequently observed Q4, P5, H6, and Q6 clusters in STM experiments. The experimental STM parameters are (a) $V_s = 1$ V and $I_t = 0.2$ nA, (b) $V_s = 1.0$ V, $I_t = 0.22$ nA, (c) $V_s = 1.0$ V, $I_t = 0.18$ nA, (d) $V_s = 0.8$ V, $I_t = 0.21$ nA, and (e) $V_s = 1.0$ V, $I_t = 0.21$ nA. f–i) DFT-simulated STM images of the clusters in (b–e).

The most frequently observed single clusters are presented in **Figure 2.** These clusters can be regular as shown in the left-hand parts of each panel, slightly distorted, or highly distorted as

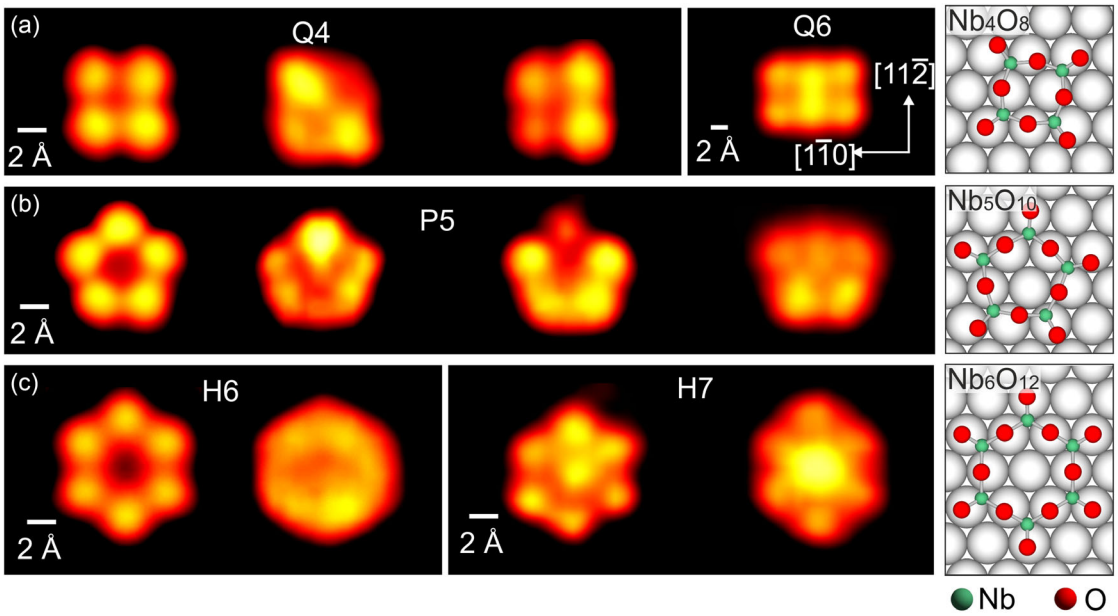

Figure 2. STM images of a variety of Nb_nO_m clusters. The most common basic units consist of units of four, five, and six Nb atoms as shown respectively in rows a) Q4 and Q6, b) P5, and c) H6. All STM images present in this figure were obtained using positive sample bias V_s approx 0.5 to 1.5 V with tunneling current I_t approx 0.1 to 1.2 nA at room temperature. The cluster morphologies are independent from the imaging conditions. Atomic models are shown in the right-hand panel in each row.

shown in the other parts of the panels. Typical STM images of the Q4 clusters are shown in Figure 2a. We most commonly observe the slightly distorted Q4 clusters. Isolated STM images of fivefold P5 clusters are shown in Figure 2b. The leftmost image of the row shows a regular pentagon, and the other images are examples of how the P5 cluster can be distorted. Examples of hexagonal clusters are shown in Figure 2c. These can either form a regular or distorted ring of 6 Nb atoms (H6), or have in their center an additional bright spot (H7).

The distortions of the clusters in Figure 2 have several possible physical origins, some of which are illustrated in Figure S3 of the Section S4 (Supporting Information). A cluster can be in different registries with respect to the Au(111) lattice. Oxygen availability in the growth environment may result in missing terminal oxygen atoms resulting in lower-coordinated Nb cations. Additional atoms such as an Au atom or a Nb atom might be trapped in the central hollow sites of a large ring, yielding additional spots in the STM images, such as the H7 cluster in Figure 2c. There is also the possibility that Nb atoms are located in the Au surface layer at the cluster periphery.

The basic units of the Q4 and P5 clusters can merge to form larger clusters. Two Q4 clusters joined at their corners are shown in **Figure 3**a where the corner atom is either shared to form a 2Q7 cluster, or not to form a 2Q8 cluster. Edge sharing of Q4 clusters results in rectangular cluster geometries, as shown in Figure 3b. The Q6, Q8, and Q10 clusters are observed relatively frequently. These rectangular clusters align their long direction epitaxially with the three <112> surface substrate directions (Section S2 and Figure S1, Supporting Information). This enables the formation of threefold corner-sharing Q cluster assemblies, as shown in Figure 3c. Figure 3d shows a row of P5 clusters that have formed pairs, by either sharing an edge (2P8) or a corner (2P9). When the P5 clusters are sufficiently close to each other they can form a bond without sharing any Nb atoms, resulting in 2P10 clusters. Figure 3e,f shows various clusters that have at their core three edge-sharing pentagons. The larger clusters from 3P12 onward also incorporate Q clusters in a similar process to those shown in Figure 3c. Figure 3g shows corner-bonded clusters, where one is assembled from two P and one Q units (2P14) and the other from three P units (3P15). We do not observe the hexagonal H-type units forming into larger cluster assemblies.

2.2. Atomic Structure of Nb_nO_m Clusters

To analyze the atomic structure of the clusters we compare our experimental STM images with DFT simulations. There is a good qualitative match between the simulated and experimental images of the Q4, P5, and H6 clusters, as shown in the STM images in Figure 1b–e and the DFT simulations in Figure 1f–i. Quantitative evaluation using comparators such as epitaxial orientation with respect to the Au(111) substrate and interatomic distances are also well-correlated.

This qualitative agreement gives us confidence in the structural solutions of these clusters (right-hand panels in Figure 2). The Q4 cluster is an eight-membered ring of alternating Nb and O atoms with a terminal O atom attached to each Nb. This results in a Nb_4O_8 cluster with NbO_2 stoichiometry. The Q4 cluster has a preferred epitaxial relationship with the Au(111) substrate. The Nb atoms are preferentially located at the threefold hollow sites of Au(111) and the O atoms are located on top sites. There is a slight offset from the center of the sites due to a structural relaxation related to strain relief in the Nb-O bonds. Hundreds of line scan measurements from the STM images

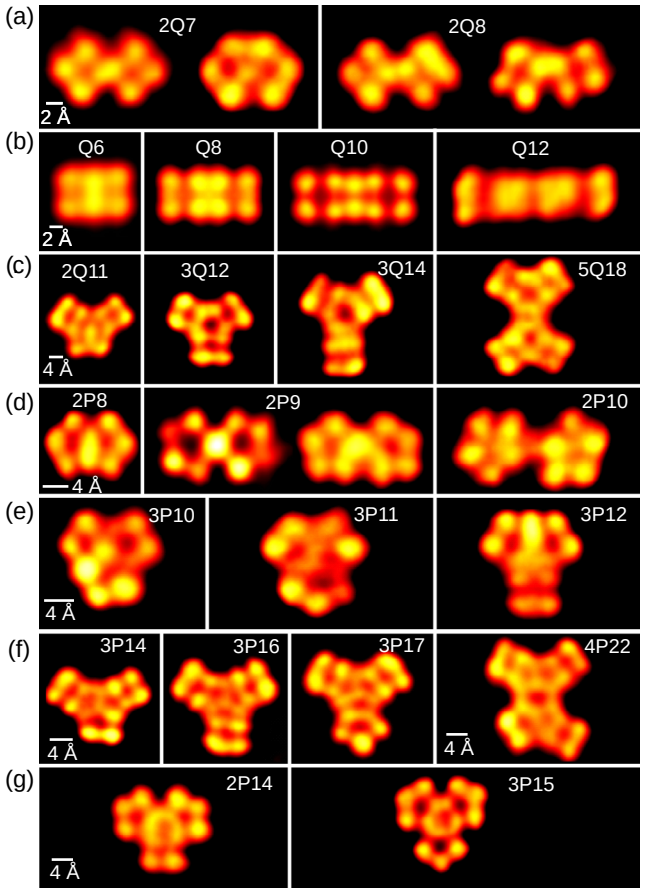

Figure 3. Small units can assemble to form larger clusters. a–c) Larger clusters based on the Q4 units. d–g) Larger clusters based on the P5 rings. The experimental STM parameters are $V_s = 0.8$ V to 1.0 V, $I_t = 0.18$ nA to 1 nA. The structure of the clusters does not vary based on the conditions under which they are imaged.

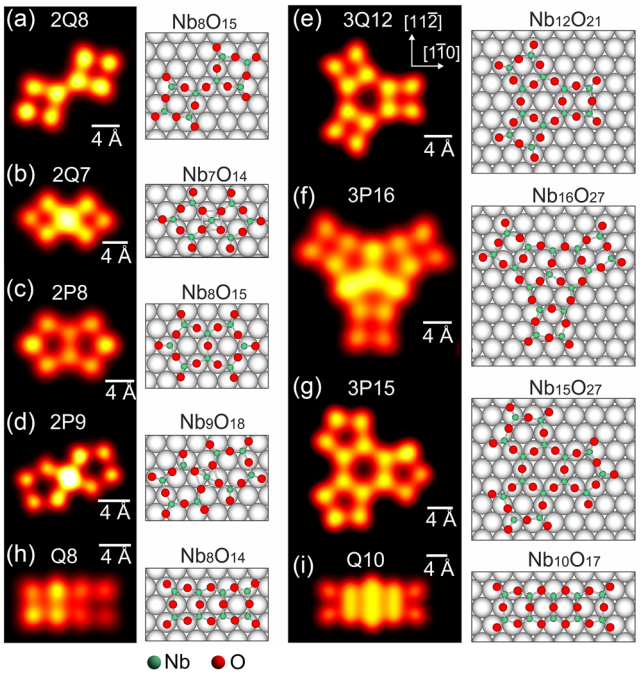

Figure 4. Structural solutions of large clusters assembled from structural units Q4 and P5. a,b) Clusters assembled from two Q4 units via a) corner-bonding and b) corner-sharing. c,d) Clusters assembled from two P5 clusters via c) edge-sharing and d) corner-sharing. e–g) Large clusters assembled from three Q4 or P5 units. h,i) Rectangular clusters composed of several Q4 units. The left-hand panels are simulated STM images using DFT and the right-hand panels are their atomic models ($E - E_F = +1$ V, distance from the center of the first Au substrate plane is 6 Å).

taken along the [1$\bar{1}$0] direction for the Q4 cluster show a distance of 3.74 ± 0.06 Å between two adjacent Nb maxima. The equivalent distance is 3.5 Å between the two maxima in the DFT simulated STM image. We have also carried out measurements between the Nb image maxima for the P5 and H6 clusters. For the P5 clusters the experimental STM measurement is 4.0 ± 0.1 Å compared with a value of 3.7 Å from the simulations, representing 8.1% difference. For the H6 clusters the experimental STM measurement is 3.80 ± 0.10 Å compared with a value of 3.6 Å from the simulations, representing a 5.6% difference. The small errors between the experiments and the simulations may originate from differences in the temperature of simulation and experiment, calibration errors of the STM piezo scanner, or the finite tip radius in the experiments, but may also result from the Tersoff–Hamann approximation used in image simulations. In any event, we consider the match between simulation and experiment to be sufficiently close to be confident of the structural solutions of the Q4, P5, and H6 clusters.

There is also a good match between experimental and simulated images of the larger clusters that form through the assembly of two or three smaller units (Figure 3 and 4). For example, a difference can be seen between the corner-bonded (**Figure 4**a) 2Q8 cluster and the corner-sharing (Figure 4b) 2Q7 cluster. Even the large clusters (Figure 4e–g) can be accurately simulated, although here we are limited by the finite unit cell size of the simulated images. It is also worth noting that the substrate in the experiments may be not as regular as the ideal Au(111) termination used in the simulations.

2.3. DFT Studies of the Structure and Stability of the Nb_nO_m Clusters

Considering the variety of observed cluster sizes (number n of Nb atoms in a cluster), a large span of possible stoichiometries (different numbers m of O atoms for each cluster size n), and a multitude of structural isomers (alternative atomic configurations for each Nb_nO_m composition), we conducted our computational study in three complementary ways. First, we focused on clusters of a fixed stoichiometry (e.g., Nb_6O_{11}) and linked the relative stability of a large variety of isomers obtained from global optimization to the fine details of their atomic structures. Then, we considered only the most stable isomers of the small clusters ($n = 4-6$) of different stoichiometries ($2n-2 \leq m \leq 2n+1$), for which we estimated the stability under the experimental oxygen UHV conditions. Finally, we turned to several mid- and large-sized particles ($n = 8-16$) with structures deduced from the experimental results and estimated their stabilities relative to equivalent pieces of the Nb_2O_3 honeycomb monolayer.

A detailed analysis of the Nb_6O_{11} isomers, Section S5 and Figure S4 in the (Supporting Information), highlights the essential structural characteristics shared by the energetically favored isomers: a flat structure, threefold coordinated cations, and terminal oxygen atoms at the cluster edges. The most energetically stable isomers correspond very well to the frequently observed rectangular Q6 cluster, and the less stable isomers are not found among the experimentally observed particles. This suggests that for a given cluster composition we convincingly determine the structure that we are likely to observe experimentally.

We then searched for the minimum energy configurations of a large variety of small Nb_nO_m/Au(111) clusters. The atomic structures of the most stable isomers obtained from global optimization are shown in **Figure 5**, together with their formation energies per Nb cation, E_{form}. As described in Section 4.2, E_{form} is calculated relative to the (2×2) Nb_2O_3/Au(111) honeycomb monolayer, under the experimental UHV oxygen conditions ($\Delta\mu_O \approx -2$ eV) and lower E_{form} values indicate larger stability.

Due to the qualitative differences in their structures, the clusters in Figure 5 can be split into three groups, characterized by different oxygen content. A high oxygen content ($m = 2n + 1$ in clusters Nb_4O_9, Nb_5O_{11}, and Nb_6O_{13}) is systematically associated

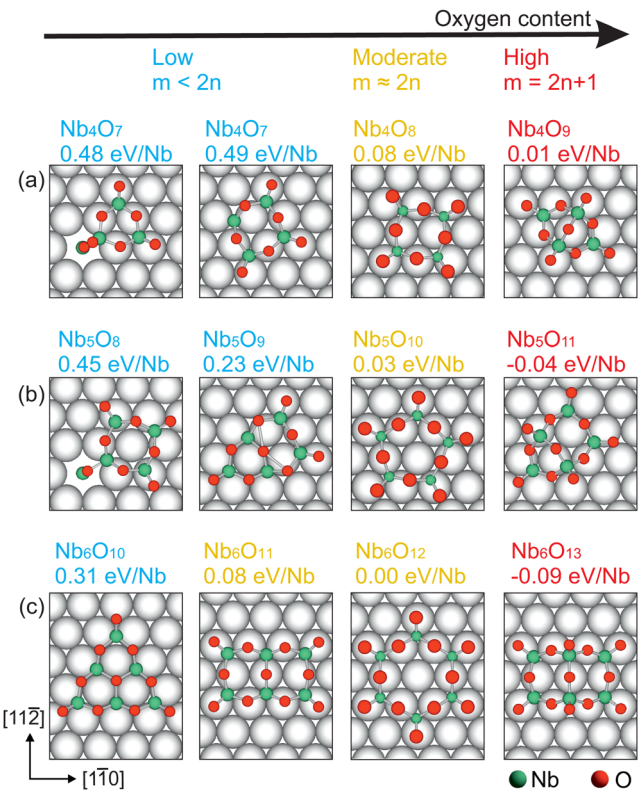

Figure 5. Top view of the most stable configurations of Nb_nO_m clusters ($n = 2$, 4, 6; $2n - 2 \leq m \leq 2n + 1$) resulting from global optimization together with their formation energies E_{form} (eV/Nb) relative to the (2×2) Nb_2O_3/Au(111) honeycomb monolayer. a) Clusters including four Nb atoms. b) Clusters consisting of five Nb atoms. c) Clusters containing six Nb atoms. The structures are classified into three groups based on oxygen content, low in blue, moderate in yellow, and high in red. The Nb_4O_8, Nb_5O_{10}, Nb_6O_{11}, and Nb_6O_{12} clusters correspond to the most frequently experimentally observed Q4, P5, Q6, and H6 particles.

with a quasi-three-dimensional particle shape. The O-rich clusters contain one or more fourfold coordinated Nb cations and the four oxygen neighbors form a tetrahedron which tends to lift the central cation away from the substrate. In spite of their favorable formation energies, such 3D cluster structures are not observed experimentally.

At moderate oxygen content (up to NbO_2 stoichiometry), the clusters remain essentially flat. The Nb cations are mostly threefold coordinated, are located in the hollow sites of the Au substrate, and are interconnected by twofold coordinated (bridging) oxygen atoms and/or bound to singly coordinated (terminal) ones. (Multi-) ring motifs with ring sizes ranging from 3 to 6 NbO members prevail, and niobyl groups are systematically found at cluster edges. The ground state Nb_4O_8, Nb_5O_{10}, Nb_6O_{11}, and Nb_6O_{12} structures display relatively low formation energies (the lowest among the flat clusters in Figure 5) and correspond to the most frequently observed Q4, P5, Q6, and H6 clusters.

At low oxygen content, structures with twofold coordinated Nb cations are present and energetically compete with those comprising buried Nb atoms. The presence of buried Nb atoms in the Au substrate has been observed experimentally[25] and is also consistent with favorable DFT dissolution energies. This is best exemplified by the two quasidegenerate Nb_4O_7 isomers in Figure 5 which show that, due to their favored position below a terminal oxygen atom, the onefold coordinated buried Nb atoms allow an increase of oxygen content in the remaining cluster, which is energetically favored in O-poor structures. However, the O-poor clusters are systematically associated with relatively large formation energies E_{form}, and do not appear among the frequently experimentally observed particles.

As far as mid- and large-sized clusters ($8 \leq n \leq 16$) are concerned, we have locally optimized structures representative of a selection of experimentally observed particles (Figure 4). The key observation is that most of their formation energies are larger than those of simple assemblies of mostly six-membered rings of similar compositions (Section S7, Figure S5 and Table S2, Supporting Information). Moreover, the energy gap between the most stable and the observed clusters increases with the cluster size. We stress that, while the choice of $\Delta\mu_O \approx -2$ eV is necessarily somewhat approximate, the reversal of cluster stability such as, e.g., to make the frequently observed $Nb_{16}O_{27}$ cluster more stable than the never observed $Nb_{16}O_{29}$ one, requires extremely O-poor conditions ($\Delta\mu_O < -3$ eV), which is inconsistent with the UHV (10^{-8} Pa) conditions in our experiments.

To summarize so far, our results show that the calculated ground state structures and compositions of small flat clusters with a moderate oxygen content, are an excellent representation of the most frequently observed particles. We also stress that, while O-rich particles with more 3D-like shapes are predicted to be more stable under the experimental conditions, they have not been observed experimentally. Finally, we demonstrate that the observed larger particles are not characterized by the lowest formation energies. These observations suggest that kinetic effects may play an important role during cluster growth and may hinder the formation of both small 3D particles and larger clusters composed of six-membered rings, typical for the HC monolayer. While an atomistic description of growth kinetics goes well beyond the scope of the present study, in the following section we will analyze the effects responsible for the enhanced

thermodynamic stability of small flat clusters with a moderate oxygen content, representative for the vast majority of the observed small particles.

2.4. Simple Model of Cohesion: Role of the Au Substrate

We have imaged a large variety of different types of Nb_nO_m/Au(111) clusters using STM, and our DFT results enable us to understand some of their common characteristics. For example, we do not experimentally observe clusters with only two or three Nb atoms, i.e., Nb_2O_x and Nb_3O_x clusters. Our DFT calculations reveal that this is because strain within the clusters plays an important role, and flat Nb_2O_x and Nb_3O_x clusters are too highly strained to be stable (Section S6, Table S1, Supporting Information). A further common theme that emerges from the calculations is that under our UHV conditions terminal O atoms stabilize the cluster structures, but result in cluster stoichiometries greater than that of the (2×2) Nb_2O_3 HC monolayer.

We now explicitly analyze the stabilization mechanism of planar clusters by the Au substrate as well as the role of the substrate in the reduction of the energy differences between structures of different stoichiometry and connectivity. These two effects are directly responsible for the coexistence of the large variety of clusters in the experiments. With the help of a simplified model of cohesion which quantifies the energetic impact of differently coordinated Nb cations, we gain further insight into the STM and DFT results and show that cluster energetic and structural characteristics have their origins in the charge transfer between the clusters and the Au substrate.

Within such a model, the cluster cohesion energy E_{coh} is expressed as a sum of contributions E_{ij} associated with each Nb cation: $E_{coh} = \Sigma_{Nb}\ E_{ij}$, where $i = 1, 2, 3, 4$ corresponds to the cation coordination number Z and $j = 0, 1$ is the number of terminal oxygen atoms among its first neighbors. The relevant E_{ij} parameters are E_{20}, E_{30}, E_{31}, E_{40}, and E_{41}, to which E_b has to be added to account for singly coordinated cations embedded in the gold surface. The E_{ij} values are derived from the DFT energies of a large number of configurations and show only a weak dependence on cluster size and stoichiometry with a typical spread in values between ± 0.1 and ± 0.2 eV. It is the consistency of the E_{ij} values across all the clusters that enables this simplified model to be reliable.

The E_{ij} values are shown in **Figure 6**a as a function of Nb coordination number Z. In the figure, the solid red line values represent the supported clusters, and the dashed black line values represent the unsupported clusters. Figure 6a shows several important trends that drive the relationship between cluster structure and stability. First, the E_{ij} parameters increase with Z, but this increase is nonlinear, a well-known behavior[28] in insulating oxides.[29] It is steep between $Z = 2$ and $Z = 3$, but it weakens as a fourth Nb-O bond is created, so that $E_2 \ll E_{31} < E_{41}$. Because $2 \times E_{31} < E_2 + E_{41}$, the stabilization of fourfold coordinated cations linked to a terminal oxygen atom becomes possible only at an oxygen content high enough to ensure that all Nb cations have at least 3 oxygen neighbors, i.e., that twofold coordinated Nb atoms are absent.

The second trend in Figure 6a is that among the three- or fourfold coordinated cations, those which have a terminal oxygen neighbor are energetically favored ($E_{31} - E_{30} \approx E_{41} - E_{40} \approx -1$ eV). The enhanced stability of these niobyl groups is consistent with their presence at the edges of the most stable flat isomers, and with the existence of branched structures with a large ratio of edge/center Nb atoms. The terminal oxygen atoms are also responsible for cluster stoichiometries larger than that of the HC monolayer. The (2×2) Nb_2O_3 HC monolayer has a stoichiometry of 1.5 with a cohesion energy per Nb equal to the E_{30} within this model. The stable flat clusters in the third column of Figure 5 all have stoichiometries of 2. Indeed, in all flat Nb_nO_m clusters composed of only threefold coordinated cations and one- or twofold coordinated anions, the stoichiometry $x = m/n$ is related to the number γ of niobyl groups by

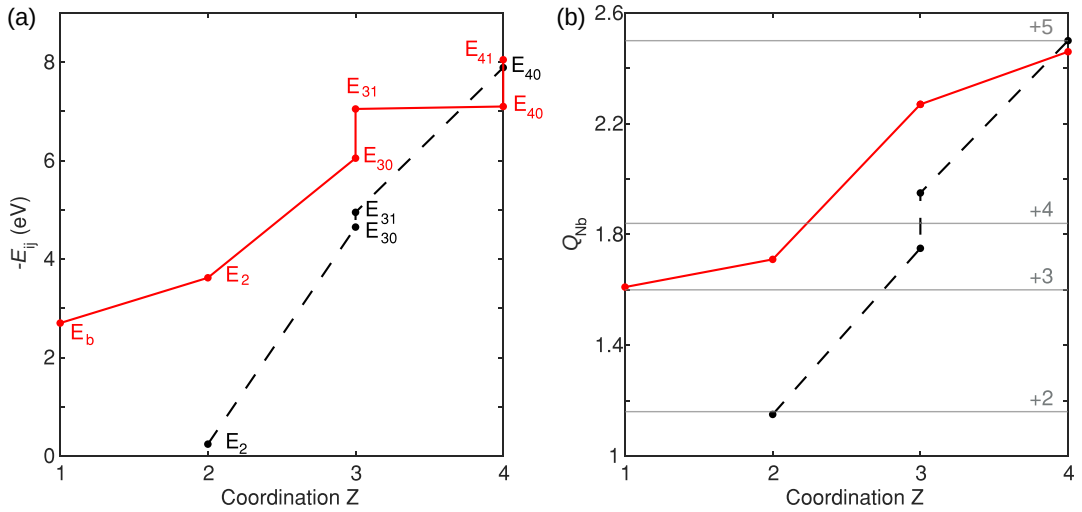

Figure 6. a) Dependence of the E_{ij} parameters (in eV) on the Nb coordination number Z in the Au-supported (solid red) and unsupported (dashed black) clusters. b) Average niobium charges Q_{Nb} on the Nb cations. As a reference, the Nb oxidation states in unsupported clusters and in the HC monolayer are indicated.

$y = 2 \times n \times (x–1.5)$. Since y cannot be larger than n in flat clusters, this condition shows that the maximum attainable stoichiometry is $x = 2$, and can be realized with n niobyl groups.

The final trend in Figure 6a concerns the presence of Nb cations buried in the gold surface (with $E_b \approx -2.7$ eV). This occurs in clusters of low stoichiometry and may be understood as an alternative to configurations with one or two twofold coordinated Nb atoms. At fixed stoichiometry, replacing a twofold coordinated Nb by a buried Nb atom induces an increase of the coordination number of a neighboring threefold coordinated Nb cation by one in a quasi-iso-energetic manner ($E_2 + E_{31} \approx E_b + E_{41}$), as found in the Nb_4O_7 cluster of Figure 5. Alternatively, replacing two twofold coordinated Nb with one buried Nb atom and one threefold coordinated Nb leads to a much more stable configuration ($E_b + E_{31} < 2 \times E_2$), as in the Nb_5O_8 cluster.

The comparison between the E_{ij} parameters of supported and unsupported clusters reported in Figure 6a provides a first hint regarding the microscopic mechanism of stabilization of the flat clusters. It shows that the energies deduced from DFT calculations on selected unsupported Nb_nO_m clusters (dashed black line in Figure 6a) are lower in absolute value than for the supported clusters and display a more rapid evolution as a function of Z. It should be noted that in comparison with their supported counterparts, the unsupported cluster atomic structures were locally relaxed to preserve their connectivity. The difference between the supported and unsupported energies is particularly well pronounced for twofold coordinated cations ($E_2^{\text{supported}} \ll E_2^{\text{unsupported}}$), remains significant for threefold coordinated ones ($E_3^{\text{supported}} < E_3^{\text{unsupported}}$, particularly when a niobyl group is involved), but hardly influences the energetics of the fourfold coordinated Nb atoms ($E_4^{\text{supported}} \approx E_4^{\text{unsupported}}$). Most importantly, the much larger difference between E_{4x} and E_{3x} in the unsupported case suggests that unsupported 3D clusters (involving principally E_{4x}) may already be favored at a much lower oxygen content (thus, lower oxygen chemical potentials) than the supported ones.

The relatively shallow gradient of E_{ij} values as a function of Z for the supported clusters significantly reduces the energy differences between clusters of different connectivity and/or stoichiometry and thus allows the coexistence of a large variety of planar configurations, as observed experimentally. More precisely, using the E_{3x} parameters leads to a particularly transparent formula for the formation energies of flat Nb_nO_m clusters of different shapes, sizes, and stoichiometries, composed of various threefold coordinated Nb cations and one- or twofold coordinated anions [stoichiometry $x = m/n$, number of edge niobyl groups $y = 2 \times n \times (x–1.5)$] relative to the supported Nb_2O_3 honeycomb monolayer ($E_{coh} = E_{30}$, $x = 1.5$, $y = 0$) as a function of the excess of oxygen chemical potential $\Delta\mu_{Ox}$

$$E_{\text{form}} = 1/n \sum_{\text{Nb}} (E_{ij} - E_{30}) - (x - 1.5)\Delta\mu_{Ox} = y/n\,[(E_{31} - E_{30}) - \Delta\mu_{Ox}/2] \quad (1)$$

Two terms are in direct competition: the stabilizing (negative, since $E_{31} < E_{30}$) cohesive energy contribution proportional to $E_{31} - E_{30}$ and the destabilizing environment-driven term proportional to $-\Delta\mu_{Ox}$ (positive, since $\Delta\mu_{Ox} < 0$). Both scale with the ratio of edge to total Nb atoms (y/n) in the cluster. In O-poor conditions (large negative $\Delta\mu_{Ox}$), the second term prevails and large objects ($y/n \ll 1$, and thus $x \approx 1.5$), such as large honeycomb monolayer patches minimize E_{form}. In contrast, under O-rich conditions (small negative $\Delta\mu_{Ox}$) the first term drives the cluster stability. In this case, minimization of E_{form} is obtained for small O-rich clusters (large y/n ratio, thus $x > 1.5$) such as the Nb_nO_{2n} cluster structures in the third column of Figure 5. A stoichiometry above 1.5 can also be achieved through small patches composed of 6-membered rings (Figure S5, Supporting Information) and also via the bi- and tripod clusters in Figure 4. Interestingly, since the experimental oxygen conditions ($\Delta\mu_{Ox} \approx -2$ eV) correspond to the transition zone where the two effects roughly compensate each other ($E_{31} - E_{30} \approx \Delta\mu_{Ox}/2$), ($E_{31} - E_{30} = -1$ eV on the Au substrate, and thus $E_{31} - E_{30} \approx \Delta\mu_{Ox}/2$) there is no strong bias toward the formation of a specific type of surface object and clusters of different sizes, shapes, and stoichiometries may coexist, in agreement with the experimental observations.

These energetic characteristics are consistent with the dramatic difference between the present observation of Nb_nO_m clusters grown on the Au surface and that of mass-selected Nb_nO_m clusters soft-landed on Cu and Au substrates from the gas phase.[17,30,31] While the terminal niobyl groups remain a universal characteristic, some three-dimensional tetrahedral structures of soft-landed clusters are observed as well as dendritic structures made of weakly bound small Nb_3O_x units. However, under annealing the soft-landed Nb_3O_x/Au clusters do not transform into flat particles similar to those observed in our STM experiments. This observation tends to confirm that the absence of 3D particles in our experiments is due to kinetic hindrance toward cluster formation on the Au substrate, as already deduced from the DFT formation energies (Figure 5).

To understand the origin of the energetic differences between the Au-supported and unsupported Nb_nO_m clusters, we analyze the Nb charges as a function of their coordination number Z. As shown in Figure 6b, the way that the charges behave is strikingly similar to those of the E_{ij} parameters in Figure 6a. We find that when Au-supported, Q_b and Q_{20} values approximately correspond to a 3+ oxidation state found in the unsupported Nb_2O_3 ML.[23] In contrast, Q_{4x} is close to a 5+ oxidation state found in unsupported tetrahedral O-rich clusters. Interestingly, the remaining threefold coordinated Nb atoms in supported flat clusters are in an oxidation state between 5+ and 4+, which is much higher than that of their counterparts in, e.g., the unsupported Nb_2O_3 ML, and is also larger than what could be deduced from the cluster stoichiometry. Such an enhancement of Nb charges occurs by means of an important electron transfer from the clusters toward the Au substrate and becomes possible due to the ability of this electronegative substrate to accept substantial negative charges (Figure S6, Supporting Information). Similar strong oxide-metal interactions and large interfacial charge transfer have been reported in TiO_x clusters supported on Au,[16] as well as in Au-supported Nb_2O_3 HC monolayers and other 2D oxide HC layers on metals.[32,33] The charge transfer was assigned to the offset between the Fermi levels of the oxide deposits and metal substrates.[23] In the present case, due to the Mott–Hubbard character of the Nb_nO_m clusters revealed by the position of the Fermi level

inside the Nb *d* band (Section S8 and Figure S7, Supporting Information), the charge transfer is associated with a depletion of the Nb *d* states and a correlated filling of empty Au states. Its variation as a function of Z results from Madelung potential effects which shift the *d* states toward higher and higher energies as the number Z of neighboring oxygen atoms increases.

To summarize this section, analyzing the cluster cohesion with local contributions associated with each cation allows us to rationalize structural features found in the observed Au-supported clusters, such as the competition between the various Nb environments in favor of threefold coordination, the existence of terminal niobyl groups, and the prevalence of flat cluster structures. The stabilizing effect of the Au substrate, which narrows the energy differences between particles of different connectivity and/or stoichiometry, is driven by charge transfer at the oxide/metal interface which induces a strong depletion of the cation states. Charge transfer to the substrate is most pronounced for the 3- (and lower-) coordinated cations, but has a much weaker effect on the 4- (and higher-) coordinated ones.

3. Conclusion

A large variety of 2D niobium oxide atomic clusters were grown on the Au(111) surface by thermally driven oxidation of metallic Nb and characterized using STM and DFT. The clusters are composed of basic units of four-, five-, and six-membered rings. The supported clusters form novel planar structures because of the strong oxide cluster–metal substrate interaction associated with the large electron transfer from the oxide clusters to the gold substrate. Under our experimental thermodynamic conditions, the coexistence of an extended range of cluster structures originates from the Au substrate interaction that narrows the formation energies of clusters consisting of threefold coordinated Nb. This report highlights the peculiarity of atomic clusters of reduced dimensionality compared with the extended continuous films. The chemical reactivity of different clusters to small molecules, such as H_2O and CO, is yet to be explored in this system and will be the subject of future investigations with relevance to catalytic applications.

4. Experimental and Theoretical Methods

Experiments: The experiments were conducted in a system under ultra-high vacuum (UHV) conditions with a base pressure of 10^{-8} Pa. A JEOL JSTM 4500XT scanning tunneling microscope (STM) was used to carry out measurements. Polished Au single crystals with a (111) termination, supplied by SurfaceNet GmbH in Germany, were cleaned through multiple sputtering and annealing cycles. Mica-supported Au(111) crystal films, produced by Agilent Technologies in the UK, were also utilized as substrates. Both versions of Au(111) substrates underwent sputtering with Ar^+ ions ranging from 0.75 to 1 kV, followed by UHV annealing at 600 °C for a period of 1.5 h. This process resulted in a herringbone reconstruction. Niobium vapor was produced using an Oxford Applied Research EGN4 e-beam evaporator with a 99.99% pure Nb rod from Goodfellow, UK. After the deposition of Nb, the Au(111) substrates were annealed between 400 and 700 °C for 15–60 min in an O_2 atmosphere ranging from 10^{-7} Pa to 10^{-6} Pa. This procedure led to the formation of niobium oxide clusters. Scanning tunneling microscopy was carried out at room temperature using etched tungsten tips.

The majority of STM images shown in this article were obtained through the method of multiple frame averaging (MFA) using the Smart Align software package. The general method and its specific application to STM are explained in the study of Jones et al.[34,35] For details regarding image processing methods, refer to the Section S1 (Supporting Information).

Theoretical Calculations: All final computational results were obtained within the plane waves density functional approach (DFT), using the spin-polarized gradient-corrected PW91 exchange-correlation functional[36] and the projector augmented wave method[37] implemented in Vienna Ab initio simulation package (VASP).[38,39] Standard niobium (including 4p electrons in the valence band) and gold, and soft oxygen (energy cutoff of 300 eV) pseudopotentials provided with VASP were used. The applicability of the soft oxygen pseudopotential was validated on several small supported clusters with results obtained with a standard pseudopotential (energy cutoff of 400 eV). Simulated STM images were obtained within the Tersoff–Hamann approximation.[40] Atomic charges were estimated according to Bader's method.[41,42]

The Au substrate was represented by a slab composed of four (111) atomic planes with the experimental in-plane lattice parameter (2.88 Å). We checked that adding a 5th metal layer resulted in negligible corrections on the reported quantities. The oxide clusters were deposited on one side of the slab and dipole corrections were applied. $(4\sqrt{3} \times 4\sqrt{3})$-Au(111) and $(5\sqrt{3} \times 5\sqrt{3})$-Au(111) surface unit cells were used in calculations of smaller (3–8 cations) and larger (9 and more cations) clusters, respectively. The Brillouin zone was sampled with a single Γ point. The atomic coordinates of all anions, cations, and Au atoms in the surface layer were allowed to relax until forces dropped below 0.01 eV Å^{-1}. Apart from the bottom-most slab layer which was kept in its bulk position, atoms in the remaining metal layers were allowed to relax only perpendicular to the surface.

Formation energies (per Nb atom) of Au-supported clusters were estimated with respect to the infinite $Nb_2O_3/(2 \times 2)$/Au(111) honeycomb monolayer[23]

$$E_{\text{form}}(Nb_nO_m) = 1/n \left[E(Nb_nO_m/Au) - n/2\, E(Nb_2O_3/Au) - \Delta n_O(\Delta\mu_O + E(O_2)/2)\right] \quad (2)$$

where $E(Nb_nO_m/Au)$, $E(Nb_2O_3/Au)$, and $E(O_2)$ are the total energies of an Au-supported Nb_nO_m cluster, of a formula unit of the Au-supported Nb_2O_3 honeycomb monolayer, and of a free oxygen molecule, respectively. $\Delta n_O = m - 3n/2$ is the difference of oxygen content in the cluster and in the Nb_2O_3 monolayer. The oxygen chemical potential $\Delta\mu_O \approx -2.0$ eV represents the annealing conditions in the experiments.

As a preliminary step, the atomic structures of small Au-supported Nb_nO_m clusters (six cations and fewer) were globally optimized with the help of a genetic algorithm (GA)[43,44] implemented in the atomic simulation environment,[45,46] similar to that employed in recent studies on free and NiAl-supported Al_2O_3 films.[47,48]

In the present case, for each composition of the supported Nb_nO_m cluster, it first consists of generating and relaxing an initial set of random cluster structures on a $(3\sqrt{3} \times 3\sqrt{3})$-Au(111) substrate. The following steps are then repeated 100 times: 1) selection of "parent" structure(s) from the previously relaxed clusters (with a bias toward the most stable ones), 2) selection and application of a genetic operator (cut-and-splice crossover or rattle mutations) to the parent structure(s) to create a new "child" cluster, which is then relaxed. Each GA run is furthermore performed 20 times, with different random seeds, to maximize the probability of finding all relevant low-energy structures. The most stable relaxed "child" structures issued from such a set of GA runs are then kept as a new generation of "parents" for the next GA iteration, and the overall convergence is monitored with the 30 most stable structures of each generation, which are locally optimized with DFT.

Such a global optimization procedure is made possible by an efficient simplified self-consistent-charge linear combination of atomic orbitals DFT scheme called density functional tight-binding (DFTB),[49] the

empirical components of which are fitted to a DFT training set using the Hotcent v1.0[50] and Tango v0.9[51] software packages. The initial training set consists of DFT energies and forces of several ordered and randomly generated Nb_nO_m clusters on the Au(111) substrate, and is further upgraded with DFT data at each subsequent step of the genetic optimization.

Supporting Information

Supporting Information is available from the Wiley Online Library or from the author.

Acknowledgements

The authors are grateful to Xiao Hu for preliminary experimental results in this area and Chris Spencer (JEOL UK) for valuable technical support.

Conflict of Interest

The authors declare no conflict of interest.

Data Availability Statement

The data that support the findings of this study are available from the corresponding author upon reasonable request.

Keywords

catalysts, density functional theory, metal-oxide interfaces, oxide clusters, scanning tunneling microscopy

Received: April 23, 2023
Revised: July 31, 2023
Published online: August 27, 2023

[1] Q. Fu, W. X. Li, Y. Yao, H. Liu, H. Y. Su, D. Ma, X. K. Gu, L. Chen, Z. Wang, H. Zhang, B. Wang, X. Bao, *Science* **2010**, *328*, 1141.
[2] F. P. Netzer, C. Noguera, *Oxide Thin Films and Nanostructures*, Oxford University Press, Oxford, UK **2021**.
[3] Q. Fu, F. Yang, X. Bao, *Acc. Chem. Res.* **2013**, *46*, 1692.
[4] Y. Liu, F. Yang, Y. Zhang, J. Xiao, L. Yu, Q. Liu, Y. Ning, Z. Zhou, H. Chen, W. Huang, P. Liu, X. Bao, *Nat. Commun.* **2017**, *8*, 14459.
[5] Y. Liu, Y. Ning, L. Yu, Z. Zhou, Q. Liu, Y. Zhang, H. Chen, J. Xiao, P. Liu, F. Yang, X. Bao, *ACS Nano* **2017**, *11*, 11449.
[6] M. S. Marshall, M. R. Castell, *Chem. Soc. Rev.* **2014**, *43*, 2226.
[7] L. Gragnaniello, F. Allegretti, R. R. Zhan, E. Vesselli, A. Baraldi, G. Comelli, S. Surnev, F. P. Netzer, *Surf. Sci.* **2013**, *611*, 86.
[8] Y. Pan, S. Benedetti, C. Noguera, L. Giordano, J. Goniakowski, N. Nilius, *J. Phys. Chem. C* **2012**, *116*, 11126.
[9] J. Schoiswohl, M. Sock, Q. Chen, G. Thornton, G. Kresse, M. Ramsey, S. Surnev, F. Netzer, *Top. Catal.* **2007**, *46*, 137.
[10] J. Schoiswohl, S. Surnev, M. Sock, S. Eck, M. G. Ramsey, F. P. Netzer, G. Kresse, *Phys. Rev. B* **2005**, *71*, 165437.
[11] J. Schoiswohl, S. Surnev, M. Sock, M. G. Ramsey, G. Kresse, F. P. Netzer, *Angew. Chem., Int. Ed.* **2004**, *43*, 5546.
[12] M. Li, E. I. Altman, *Surf. Sci.* **2014**, *619*, L6.
[13] M. Smerieri, J. Pal, L. Savio, L. Vattuone, R. Ferrando, S. Tosoni, L. Giordano, G. Pacchioni, M. Rocca, *J. Phys. Chem. Lett.* **2015**, *6*, 3104.
[14] L. Ma, M. Denk, D. Kuhness, S. Surnev, V. Mankad, G. Barcaro, A. Fortunelli, F. P. Netzer, *Surf. Sci.* **2015**, *640*, 96.
[15] G. Cabailh, J. Goniakowski, C. Noguera, J. Jupille, R. Lazzari, J. Li, P. Lagarde, N. Trcera, *Phys. Rev. Mater.* **2019**, *3*, 046001.
[16] K. R. Goodman, J. Wang, Y. Ma, X. Tong, D. J. Stacchiola, M. G. White, *J. Chem. Phys.* **2020**, *152*, 054714.
[17] M. Nakayama, M. Xue, W. An, P. Liu, M. G. White, *J. Phys. Chem. C* **2015**, *119*, 14756.
[18] J. Schoiswohl, G. Kresse, S. Surnev, M. Sock, M. G. Ramsey, F. P. Netzer, *Phys. Rev. Lett.* **2004**, *92*, 206103.
[19] L.-F. Wang, L. Xie, H.-L. Fang, Y.-F. Li, X.-B. Zhang, B. Wang, Y.-F. Zhang, X. Huang, *Spectrochim. Acta Part A Mol. Biomol. Spectrosc.* **2014**, *131*, 446.
[20] A. Fielicke, G. Meijer, G. Von Helden, *J. Am. Chem. Soc.* **2003**, *125*, 3659.
[21] Y. Yang, J. Zhou, M. Nakayama, L. Nie, P. Liu, M. G. White, *J. Phys. Chem. C* **2014**, *118*, 13697.
[22] M. Wagner, S. Surnev, M. G. Ramsey, G. Barcaro, L. Sementa, F. R. Negreiros, A. Fortunelli, Z. Dohnalek, F. P. Netzer, *J. Phys. Chem. C* **2011**, *115*, 23480.
[23] S. Wang, J. Goniakowski, C. Noguera, M. R. Castell, *Phys. Rev. B* **2019**, *100*, 125408.
[24] S. Wang, *Monolayer Oxide Films*, Oxford University, Oxford, UK **2019**.
[25] Y. Zhu, *Epitaxial Oxide Thin Films*, Oxford University, Oxford, UK **2022**.
[26] S. Wang, X. Hu, J. Goniakowski, C. Noguera, M. R. Castell, *Nanoscale* **2019**, *11*, 2412.
[27] S. Wang, X. Hu, J. Goniakowski, C. Noguera, M. R. Castell, *Adv. Mater. Interfaces* **2022**, *9*, 2102213.
[28] M. C. Desjonquères, D. Spanjaard, *Concepts in Surface Physics*, Springer, Berlin, Heidelberg, Germany **2012**.
[29] C. Noguera, *Physics and Chemistry at Oxide Surfaces*, Cambridge University Press, Cambridge, New York, Melbourne, Madrid, Cape Town, Singapore, Sao Paulo **1996**.
[30] M. Xue, M. Nakayama, P. Liu, M. G. White, *J. Phys. Chem. C* **2017**, *121*, 22234.
[31] J. Wang, Y. Ma, M. Mahapatra, J. Kang, S. D. Senanayake, X. Tong, D. J. Stacchiola, M. G. White, *Nanotechnology* **2021**, *32*, 475601.
[32] J. Goniakowski, C. Noguera, *J. Phys. Chem. C* **2019**, *123*, 9272.
[33] J. Goniakowski, C. Noguera, *J. Phys. Chem. C* **2020**, *124*, 8186.
[34] L. Jones, H. Yang, T. J. Pennycook, M. S. J. Marshall, S. Van Aert, N. D. Browning, M. R. Castell, P. D. Nellist, *Adv. Struct. Chem. Imaging* **2015**, *1*, 8.
[35] L. Jones, S. Wang, X. Hu, S. ur Rahman, M. R. Castell, *Adv. Struct. Chem. Imaging* **2018**, *4*, 7.
[36] J. P. Perdew, Y. Wang, *Phys. Rev. B* **1992**, *45*, 13244.
[37] G. Kresse, D. Joubert, *Phys. Rev. B* **1999**, *59*, 1758.
[38] G. Kresse, J. Hafner, *Phys. Rev. B* **1994**, *49*, 14251.
[39] G. Kresse, J. Furthmüller, *Phys. Rev. B* **1996**, *54*, 11169.
[40] J. Tersoff, D. R. Hamann, *Phys. Rev. Lett.* **1983**, *50*, 1998.
[41] R. F. W. Bader, *Chem. Rev.* **1991**, *91*, 893.
[42] G. Henkelman, A. Arnaldsson, H. Jónsson, *Comput. Mater. Sci.* **2006**, *36*, 354.
[43] L. B. Vilhelmsen, B. Hammer, *Phys. Rev. Lett.* **2012**, *108*, 126101.
[44] L. B. Vilhelmsen, B. Hammer, *J. Chem. Phys.* **2014**, *141*, 044711.
[45] S. R. Bahn, K. W. Jacobsen, *Comput. Sci. Eng.* **2002**, *4*, 56.
[46] A. Hjorth Larsen, J. JØrgen Mortensen, J. Blomqvist, I. E. Castelli, R. Christensen, M. Dułak, J. Friis, M. N. Groves, B. Hammer, C. Hargus, E. D. Hermes, P. C. Jennings, P. Bjerre Jensen,

J. Kermode, J. R. Kitchin, E. Leonhard Kolsbjerg, J. Kubal, K. Kaasbjerg, S. Lysgaard, J. Bergmann Maronsson, T. Maxson, T. Olsen, L. Pastewka, A. Peterson, C. Rostgaard, J. SchiØtz, O. Schütt, M. Strange, K. S. Thygesen, T. Vegge, et al., *J. Phys. Condens. Matter* **2017**, *29*, 273002.

[47] M. Van Den Bossche, C. Noguera, J. Goniakowski, *Nanoscale* **2020**, *12*, 6153.

[48] M. Van Den Bossche, J. Goniakowski, C. Noguera, *Nanoscale* **2021**, *13*, 19500.

[49] M. Elstner, D. Porezag, G. Jungnickel, J. Elsner, M. Haugk, T. Frauenheim, S. Suhai, G. Seifer, *Phys. Rev. B* **1998**, *58*, 7260.

[50] M. Van Den Bossche, *J. Phys. Chem. A* **2019**, *123*, 3038.

[51] M. Van Den Bossche, H. Grönbeck, B. Hammer, *J. Chem. Theory Comput.* **2018**, *14*, 2797.